applied sciences

MDPI

Article

Intermediate Band Studies of Substitutional V^{2+}, Cr^{2+}, and Mn^{2+} Defects in ZnTe Alloys

Jen-Chuan Tung [1,2], Bang-Wun Lin [3] and Po-Liang Liu [3,*]

1 Center for General Education, China Medical University, Taichung 402, Taiwan; jctung@mail.cmu.edu.tw
2 Program of Digital Health Innovation, China Medical University, Taichung 402, Taiwan
3 Graduate Institute of Precision Engineering, National Chung Hsing University, Taichung 402, Taiwan; sobii2164@hotmail.com
* Correspondence: pliu@dragon.nchu.edu.tw; Tel.: +886-921-820915

Received: 8 November 2020; Accepted: 10 December 2020; Published: 15 December 2020

Featured Application: This work confirms the emission band of $Cr^{2+}_{0.03}Zn_{0.97}Te$ comes from the transitions from the defect excited state to the ground state.

Abstract: We present first-principles total-energy density functional calculations to study the intermediate band states of substitutional V^{2+}, Cr^{2+}, and Mn^{2+} ions in ZnTe alloys. The intermediate band states of substitutional transition metal defects of $TM^{2+}_xZn_{1-x}Te$ (TM = V, Cr, Mn) alloys are examined as their atomic, structural, and electronic analysis. Our findings show that the scissor-corrected transitions due to Jahn-Teller effects lead to the wavelengths 2530 nm and 2695 nm in the emission spectra. Our findings agree with previously reported experimental results.

Keywords: ZnTe; infrared; transition metal; first-principles calculations

1. Introduction

The ultrashort pulse lasers of infrared (IR) light have gained great attentions for ophthalmic, surgical, dental, therapeutic, and aesthetic medical applications. The pulses from the picosecond (ps) to femtosecond (fs) require less energy to ablate biological tissues and the accuracy is in the micrometer range. At the micrometer point of the tissue through which the ultrashort pulse passes, tiny harmless carbon dioxide and water vapor bubbles are generated. Solid-state diode laser offers a number of advantages over conventional laser sources, such as reduced power consumption, better spectral purity, increased lifetime and low costs, all of which are continuously improving. It is the best and only way to promote a new high-technology development on ultrafast diode lasers. The fabrications of group II-VI laser-diodes (LDs) have become quite important for ultra-short coherent light sources. Divalent chromium doped lasers of the II-VI family emitting in the mid-infrared (mid-IR) (2–3 μm) have recently matured to the commercial continuous-wave lasers. The passively mode-locked femtosecond Cr^{2+}:ZnSe laser was first reported in 2006, generating ~100 fs pulses at up to 75 mW power around 2.5 μm wavelength [1]. The first Kerr-lens mode-locked (KLM-locked) Cr^{2+}:ZnSe laser has two distinct regimes. In the first, the output power and duration of the high-power soliton regime of Cr^{2+}:ZnSe laser is about 300 mW and 100 fs, respectively. In contrast, the output power and pulse duration of the chirped pulse regime of Cr^{2+}:ZnSe laser is about 170 mW and 1 ps, respectively [2]. In addition, another KLM-locked Cr^{2+}:ZnSe can generate 95 fs pulses with an output power as high as 40 mW around 2420 nm wavelength [3]. Furthermore, the first chirped-mirror dispersion controlled KLM Cr^{2+}:ZnSe laser using a semiconductor saturable absorbing mirror (SESAM) can generate nearly transform-limited 80 fs pulses at 80 mW output power around 2.4 μm wavelength [4].

On the other hand, Cr^{2+}:ZnS lasers have been extensively studied both experimentally and theoretically. The zinc-blende ZnS has the larger band gap of 3.8 eV, higher thermal conductivity of 27 W/mK, higher thermal shock parameter of 7.1 W/m$^{1/2}$, and lower dn/dT of 46×10^{-6} K^{-1}, compared respectively to 2.8 eV, 18 W/mK, 5.3 W/m$^{1/2}$, and 70 × 10^{-6} K^{-1} in ZnSe [5,6]. Therefore, the fabrication of Cr^{2+}:ZnS lasers has shown the promising prospect for high-power applications. The first continuous-wave (CW) tunable Cr^{2+}:ZnS laser was first introduced using the direct diode-pumping at 1.67 μm and generating 100 mW output power of the broadly CW tunable over ~280 nm around 2.3 μm wavelength [7]. Furthermore, the first mode-locked CW Cr^{2+}:ZnS laser, passively mode-locked by a multiple quantum well InAs/GaSb based SESAM, generated ~1.1 ps pulses at 125 mW of output power around 2.45 μm [8]. Recently, the first single-crystalline KLM femtosecond Cr^{2+}:ZnS laser was reported, generating high power up to 200 mW stable around 2.4 μm wavelength and clean 110 fs pulses at 180 MHz repetition rate [9]. To date, output average power up to 800 mW at 49.9 MHz repetition rate, and pulse duration as short as 34 fs at 2.4 μm wavelength have been determined experimentally using the KLM-locked femtosecond Cr^{2+}:ZnS oscillator pumped by two single-emitter InP C-Mount laser diodes [10]. Due to promising unique properties advanced Cr^{2+} doped II-VI materials for medical lasers have attracted tremendous recent attention from both fundamental and practical viewpoints and their applications have become a hot and active field in the world range wide.

In recent applications, the ZnTe crystal shows attractive detection performances at frequencies below the Reststrahlen band (<5.3 THz for ZnTe) with a broadband (FWHM = 100 nm) femtosecond (fs) laser [11]. The complex dielectric constant of materials or biological and medical research was detected using THz pulses in electro-optic crystals, but the waveform distortions of THz pulses due to effects of phase mismatch, dispersive propagation, and absorption become more severe with the increase of crystal thickness. The (110)-oriented ZnTe crystal as thick as 3 mm has proven to work for the frequency below 3 THz without remarkable distortions. In view of the difficulty in the crystal growth of <110> ZnTe wafers due to the high melting point of 1568 K and structural defects, a temperature gradient solvent method under Te-rich condition with subwavelength microstructure on the ZnTe crystal surface by reactive ion etching was performed to obtain the optical level of ZnTe crystals [12]. In this case, the analysis of the bulk resistivity under a bias voltage of 1 V indicates that ZnTe:V ($Zn_{1-x}Mn_xTe$) shows higher resistivity of 10^8–10^9 Ω·cm (200–400 Ω·cm) than intrinsic ZnTe of 50–100 Ω·cm. The manganese-doped ZnTe crystal can enhance the THz emitter and sensor by 10~19% and 17~28%, respectively. The ZnTe:V crystal can increase the detection sensitivity by 20–30%. In applications requiring the use of the copper doping in cadmium telluride (CdTe) solar cells while limiting the diffusion of copper due to copper as interstitial defects with high mobility, the Cu-doped ZnTe film was selected for the back contacts in the CdTe photovoltaic devices [13]. The CdTe photovoltaic device with a ZnTe layer shows a better open-circuit voltage of 841 mV, a higher short-circuit current of 26.7 mA/cm^2, and an external quantum efficiency as high as 17.66%. On the theoretical side, a full-potential linearized augmented plane wave (FP-LAPW) and the local orbital (LO) calculations for structural, electronic, and optical properties of zinc blende and wurtzite phases of the ZnTe indicated that the zinc blende ZnTe appears to be the most stable at room temperature [14]. The reflectivity of zinc blende and wurtzite phases of the ZnTe are about 30% and 38%, respectively, which show that the zinc blend phase ZnTe has good transmittance in the visible range, better than the wurtzite one.

For ultrashort coherent light sources, the production of transition metal-doped zinc chalcogenides has become very important. In the particular cases of ZnS, ZnSe, and ZnTe alloys individually doped with Cr^{2+}, Co^{2+}, Ni^{2+}, or Fe^{2+}, previous studies have shown that the transition metal ions in the II-VI compounds are susceptible to distortions of tetragonal symmetry [15]. Moreover, the tetragonal deformation leads to Jahn-Teller effects which further split the ground and excited states. For examples in Cr^{2+} doped ZnS, ZnSe, and ZnTe alloys the wavelengths of room-temperature emission spectra are all between 1900 and 2700 nm, suggesting the emission bands from the transitions from the

metastable excited state to the ground state. Furthermore, divalent chromium doped lasers of the II-VI family emitting in the mid-infrared (mid-IR) (2070–2420 nm) have been reported, such as Cr^{2+}:ZnS, Cr^{2+}:ZnSe, and Cr^{2+}:ZnTe. The emission-quantum yield is as high as 100% at 300K, but the transition in detail is less explainable [16]. In order to explain intermediate band states of substitutional transition metal defects in the II-VI compounds, we investigate the atomic structures, band structures and electronic structures of $TM^{2+}{}_xZn_{1-x}Te$ (TM = V, Cr, Mn) alloys, in which the transition metal ion TM^{2+} is distributed on the substitutional site.

2. Theoretical Approach

We report on ab initio calculations to study the intermediate band states of substitutional transition metal defects in $TM^{2+}{}_xZn_{1-x}Te$ (TM = V, Cr, Mn) alloys. Our ab initio studies were based on the density functional theory (DFT) methods and calculated with the Vanderbilt ultrasoft pseudopotentials (USPPs) using the Cambridge serial total energy package (CASTEP) [17,18]. The utilized USPPs to efficiently treat ion-electron interactions derived from the projector augmented wave (PAW) method and the generalized gradient approximation (GGA) with the Perdew-Wang (PW91) exchange-correlation functional [19,20]. The electronic configurations for the valence electrons are V: $3s^23p^64s^23d^3$, Cr: $3s^23p^64s^13d^5$, Mn: $4s^23d^5$, Zn: $4s^23d^{10}$, and Te: $4d^85p^4$. The ZnTe (space group: 216 *F-43m*) and $TM^{2+}{}_xZn_{1-x}Te$ (TM = V, Cr, Mn) alloys were constructed using bulk crystalline configurations with discrete TM^{2+} compositions of 25% and 3% (or x = 0.25 and x = 0.03). The structural properties of $TM^{2+}{}_{0.25}Zn_{0.75}Te$, and $TM^{2+}{}_{0.03}Zn_{0.97}Te$ were modeled by substituting one TM^{2+} ion on the Zn site within an 8-atom and 64-atom zinc-blende lattice unit cells, respectively. The 8-atom zinc-blende ZnTe and $TM^{2+}{}_{0.25}Zn_{0.75}Te$ (TM = V, Cr, Mn) models and 64-atom zinc-blende $Cr^{2+}{}_{0.03}Zn_{0.97}Te$ model are shown in Figure 1. The Brillouin zones were performed using a $4 \times 4 \times 4$ ($2 \times 2 \times 2$) Monkhorst-Pack grid and a 400 eV (150 eV) energy cutoff in $TM^{2+}{}_{0.25}Zn_{0.75}Te$ ($TM^{2+}{}_{0.03}Zn_{0.97}Te$). The highest occupied Kohn–Sham orbitals (HOMO) and lowest unoccupied Kohn–Sham orbitals (LUMO) have been used to analyze the intermediate band states of substitutional transition metal defects in $TM^{2+}{}_xZn_{1-x}Te$ (TM = V, Cr, Mn) alloys. Recent theoretical work confirms that the infrared light emission of 0.852 eV derived from first-principles theoretical models is close to the value 0.842 eV of experimental photoluminescence (PL) defect-peak observations of the twist–bonded dislocation network [21].

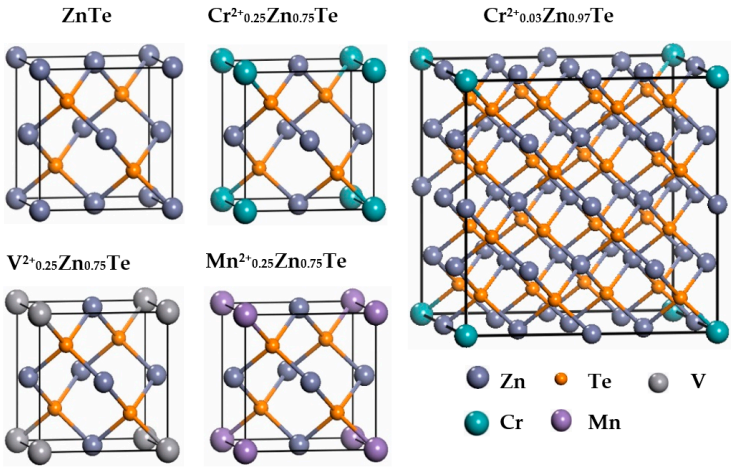

Figure 1. Atomistic representations of 8-atom ZnTe, $V^{2+}{}_{0.25}Zn_{0.75}Te$, $Cr^{2+}{}_{0.25}Zn_{0.75}Te$, $Mn^{2+}{}_{0.25}Zn_{0.75}Te$, and 64-atom $Cr^{2+}{}_{0.03}Zn_{0.97}Te$ models. The atoms are represented by spheres: Zn (gray, dark), Te (yellow), V (gray, light), Cr (green), and Mn (purple).

3. Intermediate Band States

The geometry optimizations of ZnTe and $TM^{2+}{}_{0.25}Zn_{0.75}Te$ (TM = V, Cr, Mn) through DFT-GGA calculations were shown in Figures 2–4. We clearly see that the HOMO levels of ZnTe are localized on

the Te atoms in the left panel of Figure 2. The LUMO isosurfaces are significantly different from the HOMO isosurfaces. The LUMO levels of ZnTe are not only around Te atoms but also around Zn atoms. In the right panel of Figure 2 it can be clearly seen that |1>, |0>, |−1>, and |−2> levels of $V^{2+}{}_{0.25}Zn_{0.75}Te$ are in the bottom of the forbidden gap of the ZnTe or between the valence E_0 and conduction E_1 band of the ZnTe. The extremely narrow band gap cannot emit in the IR laser.

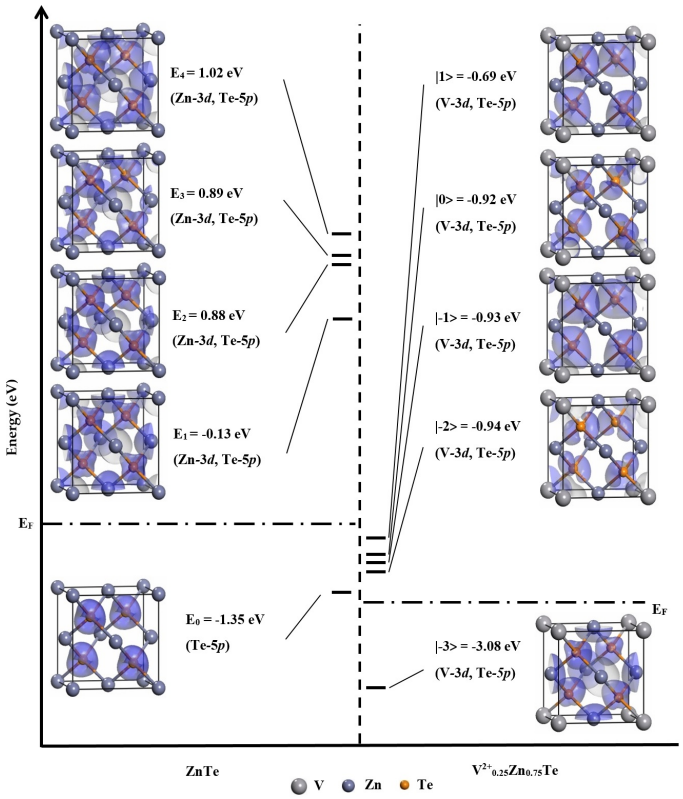

Figure 2. Left (Right) panel: HOMO and LUMO slab isosurfaces of 8-atom ZnTe ($V^{2+}{}_{0.25}Zn_{0.75}Te$) cells arranged by energy and denoted by the shade of purple. The atoms are represented by spheres: V (gray, light), Zn (gray, dark), and Te (yellow).

Furthermore, the eight-atom zinc-blende ZnTe and $Cr^{2+}{}_{0.25}Zn_{0.75}Te$ models are shown in Figure 3 The results in the right panel of Figure 3 inform that the Cr^{2+} ions in the ZnTe compounds lead to Jahn-Teller effects which further split the ground and excited states. It can be seen that $Cr^{2+}{}_{0.25}Zn_{0.75}Te$ is a good laser gain medium with the multi-level system, which the upper |1>, |0>, |−1>, and |−2> levels may lead to a significant population inversion.

Moreover, the eight-atom zinc-blende ZnTe and $Mn^{2+}{}_{0.25}Zn_{0.75}Te$ models are shown in Figure 4. It can be clearly seen that there is not any level of $Mn^{2+}{}_{0.25}Zn_{0.75}Te$ in the forbidden gap of the ZnTe. The $Mn^{2+}{}_{0.25}Zn_{0.75}Te$ is a two-level system, where it is hard to achieve population inversion in the two-level system.

Figure 5a shows a two-level system with the ground state 0 and the excited state 3 indicating that the rate of absorption is the same as one of spontaneous emission or stimulated emission. It is hard to achieve population inversion in the two-level system. The idea laser gain medium with the multi-level system, such as four-level system as shown in Figure 5b, may lead to a significant population inversion. The stimulated emission occurs from level 2 to level 1 and is the basis of photon amplification and the basic mechanism of the laser action. Our eight-atom $Cr^{2+}{}_{0.25}Zn_{0.75}Te$ model is the only one of the four-level system where the population inversion could be achieved.

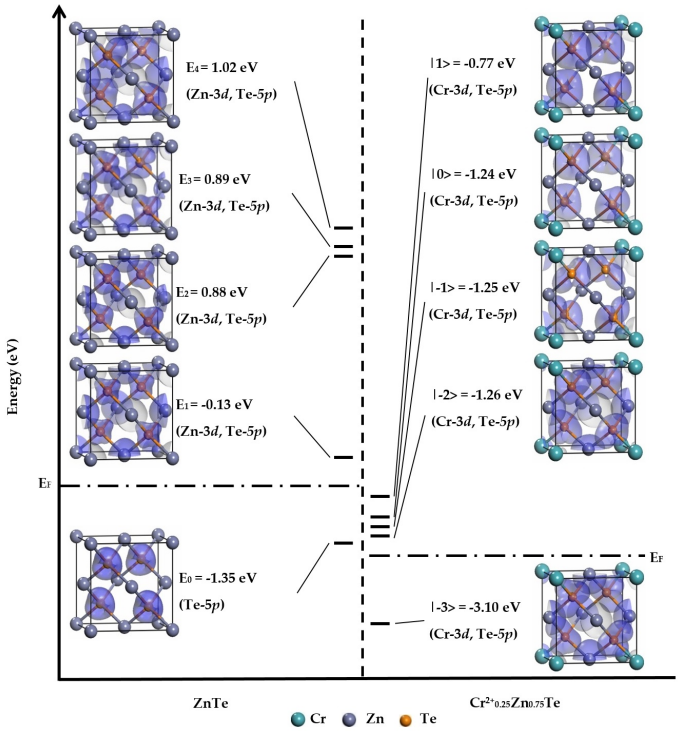

Figure 3. Left (Right) panel: HOMO and LUMO slab isosurfaces of 8-atom ZnTe ($Cr^{2+}{}_{0.25}Zn_{0.75}Te$) cells arranged by energy and denoted by the shade of purple. The atoms are represented by spheres: Cr (green), Zn (gray, dark), and Te (yellow).

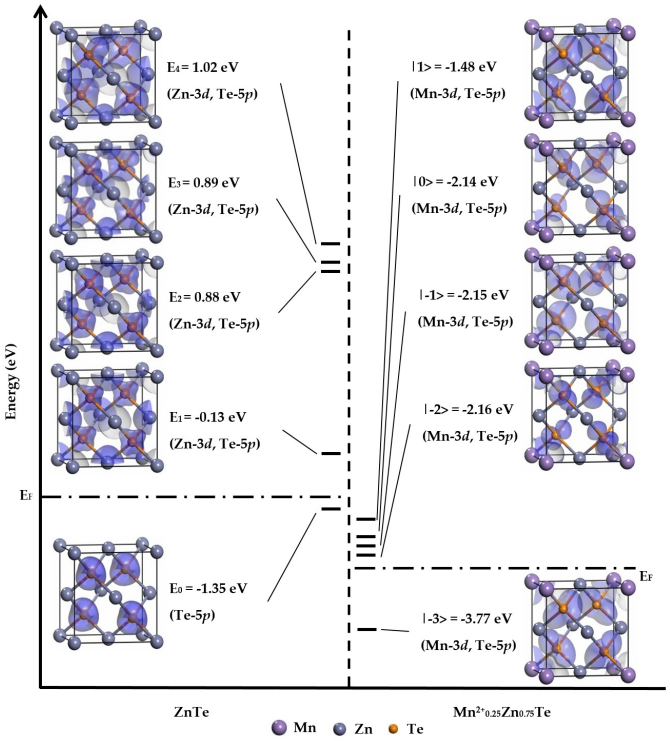

Figure 4. Left (Right) panel: HOMO and LUMO slab isosurfaces of 8-atom ZnTe ($Mn^{2+}{}_{0.25}Zn_{0.75}Te$) cells arranged by energy and denoted by the shade of purple. The atoms are represented by spheres: Mn (purple), Zn (gray, dark), and Te (yellow).

The calculated ground state structures for ZnTe and $TM^{2+}{}_{0.25}Zn_{0.75}Te$ (TM = V, Cr, Mn) and their optical properties (band gaps) are summarized in Table 1. The lattice constants of strain relaxed lattices of $V^{2+}{}_{0.25}Zn_{0.75}Te$, $Cr^{2+}{}_{0.25}Zn_{0.75}Te$, $Mn^{2+}{}_{0.25}Zn_{0.75}Te$ are, respectively, 0.16%, 0.48%, and 0.16% larger than the one of ZnTe. The data also show the band gap of $TM^{2+}{}_{0.25}Zn_{0.75}Te$ decreases as the dopant atom is substituted by ZnTe in the alloy, yielding a long-wavelength emission or a narrow band gap from the TM^{2+} ion. The calculated band gap of ZnTe of 1.23 eV is in excellent agreement with the other theoretical value of 1.4 eV [22]. We note that the band gaps of $V^{2+}{}_{0.25}Zn_{0.75}Te$ and $Cr^{2+}{}_{0.25}Zn_{0.75}Te$ are somewhat lower than other theoretical gaps of $V_{0.25}Zn_{0.75}Te$ and $Cr_{0.25}Zn_{0.75}Te$ obtained by FP-LAPW calculations without using the two-valent chromium and vanadium [23,24], respectively, showing that the band gaps are strongly influenced by the two-valent species.

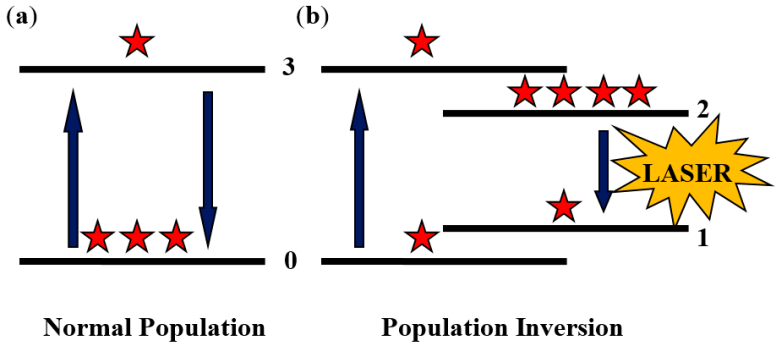

Figure 5. Schematic illustration of the normal population (**a**) and population inversion (**b**). Upward arrows show optical pumping which make electrons (solid stars) to rise from a lower energy level 0 to a higher one 3. Downward arrows indicate electrons emit photons when they relax from excited states 3 or 2 to lower states 1 or 0.

Table 1. The lattice constants of optimized atomic structures of ZnTe and $TM^{2+}{}_{0.25}Zn_{0.75}Te$ (TM = V, Cr, Mn) fit other theoretical values. The corresponding band gaps are compared with other calculated values.

Compounds	Lattice Constant (Å)		Energy Gap (eV)	
ZnTe	6.19	6.09 [a]	1.23	1.4 [a]
$V^{2+}{}_{0.25}Zn_{0.75}Te$	6.20	6.22 [b]	0.25	0.33 [b,*]
$Cr^{2+}{}_{0.25}Zn_{0.75}Te$	6.22	6.22 [c]	0.49	0.77 [c,*]
$Mn^{2+}{}_{0.25}Zn_{0.75}Te$	6.20		0.68	

[a] Ref. [22]; [b] Ref. [23]; [c] Ref. [24]; * Note: bang gaps of neutral species, $V_{0.25}Zn_{0.75}Te$ and $Cr_{0.25}Zn_{0.75}Te$.

Previous studies reported that the infrared femtosecond lasers using transition metals doped II–VI materials with transition metal compositions up to 3% [25–27]. Therefore, our models with transition metals compositions of 25% cannot refer to reality. In order to compare with the experimental observations of transition metals Cr^{2+} doped ZnTe materials with low concentration we modeled 64-atom zinc-blende ZnTe and $Cr^{2+}{}_{0.03}Zn_{0.97}Te$. In fact, as we will show below, the use of the 64-atom large cell allows us to prove that the ZnTe with Cr^{2+} dopants as low as 3%, not included in the V^{2+}- and Mn^{2+}-doped ZnTe, is nearly identical within the four-level system as an 8-atom small cell. The reasons which we have not included doping with V^{2+} and Mn^{2+} for the larger cell are as following: (a) no level of $Mn^{2+}{}_{0.25}Zn_{0.75}Te$ in the forbidden gap of the ZnTe, showing a two-level system and limiting to the population inversion, (b) the defect levels of $V^{2+}{}_{0.25}Zn_{0.75}Te$ in the bottom of the forbidden gap of the ZnTe, showing that the extremely narrow band gap cannot emit in the IR laser, (c) the IR laser emitted in the small cell of $Cr^{2+}{}_{0.25}Zn_{0.75}Te$, suggesting that IR laser will be emitted in the large unit of $Cr^{2+}{}_{0.03}Zn_{0.97}Te$. According to experimental observations [1–10,15,16], it is perhaps not surprising that the II–VI compounds doped with transition metal Cr^{2+} are mature laser materials.

The HOMO and LUMO of ZnTe and $Cr^{2+}_{0.03}Zn_{0.97}Te$ were calculated as shown in Figure 6. We can be clearly seen that |1>, |0>, |−1>, and |−2> levels of $Cr^{2+}_{0.03}Zn_{0.97}Te$ are in the forbidden gap of the ZnTe. The fundamental gap between the conduction band and defect levels can be corrected with a "scissor operator" to match the photoluminescence (PL) peaks due to the well-known bandgap underestimation of DFT calculations. The calculated band gap of 0.94 eV is corrected by the scissor correction (the scissors operator is 1.63 eV) to approach the PL emission in the 2.57 eV spectral region. |0> and |−1> metastable excited states to E_0 ground state are scaled up to 0.49 eV and 0.46 eV, which the wavelengths are 2530 nm and 2695 nm, respectively. Our results agree with previously reported experimental results [15].

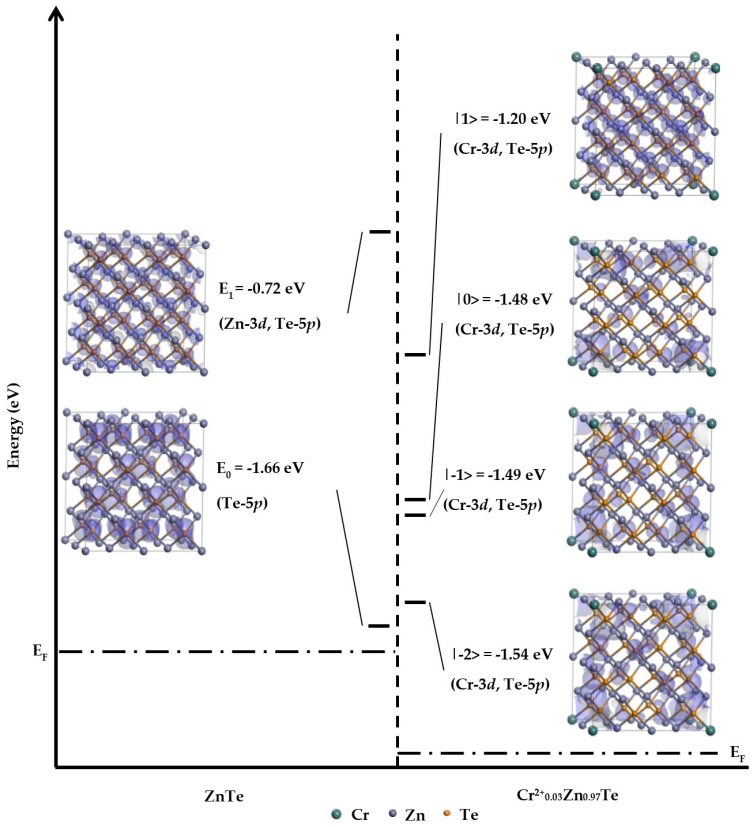

Figure 6. Left (Right) panel: HOMO and LUMO slab isosurfaces of 64-atom ZnTe ($Cr^{2+}_{0.03}Zn_{0.97}Te$) cells arranged by energy and denoted by the shade of purple. The atoms are represented by spheres: Cr (green), Zn (gray, dark), and Te (yellow).

In order to understand how defects in ZnTe alloys we calculate the formation energy and defect formation energy of ZnTe and $TM^{2+}_{0.25}Zn_{0.75}Te$ (TM = V, Cr, Mn). The formation energy E_f can be written as

$$E_f = E_{tot} - \Sigma\, n_i \mu_i, \quad (1)$$

where E_{tot} is the total energy of bulk ZnTe; n_i and μ_i are the number of atoms and the chemical potential of the ith constituent of the bulk. The defect formation energy E_d can be determined by the difference of the formation energies between bulks ZnTe and $TM^{2+}_{0.25}Zn_{0.75}Te$ (TM = V, Cr, Mn) and given by

$$E_d = E_{tot\_defect} - E_{tot} - n_d\,(\mu_d - \mu_{Zn}), \quad (2)$$

where E_{tot_defect} is the total energy of bulk $TM^{2+}_{0.25}Zn_{0.75}Te$ (TM = V, Cr, Mn). n_d is the number of TM atoms. μ_d and μ_{Zn} are the chemical potential of TM and Zn, respectively. Table 2 lists the results of the formation energy and the defect formation energy for ZnTe and $TM^{2+}_{0.25}Zn_{0.75}Te$ (TM = V, Cr, Mn).

We find that the V^{2+} ion preferentially occupies the Zn site, leading to the minimum defect formation energy of 2.441 eV. In contrast, Cr^{2+} ion occupies the Zn site and becomes more unstable due to the maximum defect formation energy of 3.158 eV.

Table 2. Formation and defect formation energies of ZnTe and $TM^{2+}{}_{0.25}Zn_{0.75}Te$ (*TM* = V, Cr, Mn).

	Formation Energy (eV)	Defect Formation Energy (eV)
ZnTe	−3.765	0
$V^{2+}{}_{0.25}Zn_{0.75}Te$	−1.325	2.441
$Cr^{2+}{}_{0.25}Zn_{0.75}Te$	−0.608	3.158
$Mn^{2+}{}_{0.25}Zn_{0.75}Te$	−0.901	2.864

4. Conclusions

The intermediate band states of substitutional transition metal defects in $TM^{2+}{}_{x}Zn_{1-x}Te$ (*TM* = V, Cr, Mn) alloys were studied by first-principles calculations. By studying the atomic structures, band structures and electronic structures of 8-atom and 64-atom zinc-blende lattice unit cells, we found that the Cr^{2+} ion in the ZnTe compounds leads to Jahn-Teller effects which further split the ground and excited states. Our scissor-corrected wavelengths of the transitions from the metastable excited state to the ground state are 2530 nm and 2695 nm. Our results agree with the corresponding observed experiments [15]. In this case we have succeeded in explaining the intermediate band states of substitutional transition metal defects in the II–VI compounds, which enable us to determine the emission spectra of next generation diode lasers.

Author Contributions: Conceptualization, J.-C.T. and P.-L.L.; methodology, B.-W.L.; validation, B.-W.L.; formal analysis, J.-C.T., B.-W.L. and P.-L.L.; investigation, B.-W.L.; writing—original draft preparation, J.-C.T. and P.-L.L.; writing—review and editing, J.-C.T. and P.-L.L.; supervision, P.-L.L. All authors have read and agreed to the published version of the manuscript.

Funding: This research was funded by Ministry of Science and Technology (MOST), Taiwan, grant numbers 109-2221-E-005-042 and 108-2221-E-005-001.

Acknowledgments: Computational studies were performed using the resources of the National Center for High Performance Computing, Taiwan.

Conflicts of Interest: The authors declare no conflict of interest.

References

1. Sorokina, I.T.; Sorokin, E.; Carrig, T. Femtosecond Pulse Generation from a SESAM Mode-Locked Cr: ZnSe Laser. In Proceedings of the Conference on Lasers and Electro-Optics, San Jose, CA, USA, 5–10 June 2006.
2. Sorokin, E.; Sorokina, I.T. Ultrashort-pulsed Kerr-lens modelocked Cr: ZnSe laser. In Proceedings of the European Conference on Lasers, Munich, Germany, 15–19 June 2009.
3. Cizmeciyan, M.N.; Cankaya, H.; Kurt, A.; Sennaroglu, A. Kerr-lens mode-locked femtosecond Cr^{2+}: ZnSe laser at 2420 nm. *Opt. Lett.* **2009**, *34*, 3056. [CrossRef] [PubMed]
4. Sorokina, I.T.; Sorokin, E. Chirped-Mirror Dispersion Controlled Femtosecond Cr: ZnSe Laser. In Proceedings of the Advanced Solid State Photonics, Vancouver, BC, Canada, 29–31 January 2007.
5. Trager, F. Lasers and Coherent Light Sources. In *Springer Handbook of Lasers and Optics*, 2nd ed.; Frank, T., Ed.; Springer: Dordrecht, The Netherlands, 2012; Volume 11, pp. 749–750.
6. Majid, E.-Z.; Irina, T.-S. *Mid-Infrared Coherent Sources and Applications*; Springer: Dordrecht, The Netherlands, 2005; pp. 236, 241.
7. Sorokina, I.-T.; Sorokin, E.; Mirov, S.; Fedorov, V.; Badikov, V.; Panyutin, V.; Lieto, A.-D.; Tonelli, M. Continuous-wave tunable Cr^{2+}: ZnS laser. *Appl. Phys. B* **2002**, *74*, 607. [CrossRef]
8. Sorokina, I.T.; Sorokin, E.; Carrig, T.-J.; Schaffers, K. *A SESAM Passively Mode-Locked Cr:ZnS Laser*; The Optical Society: Washington, DC, USA, 2006.
9. Sorokin, E.; Tolstik, N.; Sorokina, I.-T. Femtosecond operation and self-doubling of Cr: nS laser. In Proceedings of the Nonlinear Optics: Materials, Fundamentals and Applications, Kauai, HI, USA, 17–22 July 2011; p. NThC1.

10. Nagl, N.; Gröbmeyer, S.; Pötzlberger, M.; Pervak, V.; Krausz, F.; Mak, K.F. Directly Diode-Pumped Few-Optical-Cycle Cr: ZnS Laser at 800 mW of Average Power. In Proceedings of the Conference on Lasers and Electro-Optics, San Jose Convention Center, San Jose, CA, USA, 10–15 May 2020; IEEE: San Jose, CA, USA, 2020.
11. Wu, B.; Cao, L.; Zhang, Z.; Fu, Q.; Xiong, Y. Terahertz Electro-Optic Sampling in Thick ZnTe Crystals Below the Reststrahlen Band With a Broadband Femtosecond Laser. *IEEE Trans. Terahertz. Sci. Technol.* **2018**, *8*, 305. [CrossRef]
12. Xu, Y.-D.; Dong, J.-P.; Xiao, B.; Zhang, B.-B.; Teichert, C.; Jie, W. Tailoring structure imperfection in ZnTe bulk crystals and improving the terahertz response. In Proceedings of the International Symposium on Ultrafast Phenomena and Terahertz Waves 2018, Changsha, China, 23–26 April 2018.
13. Kindvall, A.; Munshi, A.; Shimpi, T.; Danielson, A.; Sampath, W.S. Effect of Process Temperature and Copper Doping on the Performance of ZnTe: Cu Back Contacts in CdTe Photovoltaics. *IEEE Xplore* **2019**, 19321930.
14. Aazi, M.; Atmani, E.H.; Fazouan, N.; Bziz, I.; Adil, E.-S. *Ab-initio* Study of Structural, Electronic and Optical Properties of ZnTe at Wurtzite and Zinc Blende Phases. In Proceedings of the 2019 7th International Renewable and Sustainable Energy Conference (IRSEC), Agadir, Morocco, 27–30 November 2019; IEEE: New York, NY, USA, 2019.
15. DeLoach, L.D.; Page, R.H.; Wilke, G.D.; Payne, S.A.; Krupke, W.F. Transition Metal-Doped Zinc Chalcogenides: Spectroscopy and Laser Demonstration of a New Class of Gain Media. *IEEE J. Quantum Electron.* **1996**, *32*, 885–895. [CrossRef]
16. Bluiett, A.G.; Hommerich, U.; Shah, R.T.; Trivedi, S.B.; Kutcher, S.W.; Wang, C.C. Observation of Lasing from Cr^{2+}: CdTe and Compositional Effects in Cr^{2+}-Doped II-VI Semiconductors. *J. Electron. Mater.* **2002**, *31*, 806–810. [CrossRef]
17. Payne, M.C.; Tatter, M.P.; Allan, D.C.; Arias, T.A.; Joannopoulos, J.D. Iterative minimization techniques for *ab initio* total-energy calculations: Molecular dynamics and conjugate gradients. *Rev. Mod. Phys.* **1992**, *64*, 1045. [CrossRef]
18. Milman, V.; Winkler, B.; White, J.A.; Pickard, C.J.; Payne, M.C.; Akhmatskaya, E.V.; Nobes, R.H. Electronic Structure, Properties, and Phase Stability of Inorganic Crystals: A Pseudopotential Plane-Wave Study. *Int. J. Quantum Chem.* **2000**, *77*, 895. [CrossRef]
19. Perdew, J.P.; Wang, Y. Pair-distribution function and its coupling-constant average for the spin-polarized electron gas. *Phys. Rev. B* **1992**, *13244*, 45. [CrossRef] [PubMed]
20. Perdew, J.P.; Chevary, J.A.; Vosko, S.H.; Jackson, K.A.; Pederson, M.R.; Singh, D.J.; Fiolhais, C. Atoms, molecules, solids, and surfaces: Applications of the generalized gradient approximation for exchange and correlation. *Phys. Rev. B* **1992**, *6671*, 46. [CrossRef] [PubMed]
21. Hsin, C.-L.; Teng, H.-S.; Lin, H.-Y.; Cheng, T.-H.; Cheng, C.-C.; Liu, P.-L. Electronic structure and infrared light emission in dislocation-engineered silicon. *IEEE Trans. Nanotechnol.* **2015**, *14*, 399–403. [CrossRef]
22. Reshak, A.H.; Auluck, S. *Ab initio* calculations of the electronic, linear and nonlinear optical properties of zinc chalcogenides. *Physica B* **2007**, *388*, 34–42. [CrossRef]
23. Liu, Y.; Liu, B.-G. Ferromagnetism in transition-metal-doped II–VI compounds. *J. Magn. Magn. Mater.* **2006**, *307*, 245–249. [CrossRef]
24. Liu, Y.; Liu, B.G. *First-principles* study of half-metallic ferromagnetism and structural stability of $Cr_xZn_{1-x}Te$. *J. Phys. D* **2007**, *40*, 6791–6796. [CrossRef]
25. Hou, S.; Zhang, X.; Mao, H.; Wang, J.; Zhu, Z.; Jing, W. Photoluminescence and XPS investigations of Cu^{2+} -doped ZnS quantum dots capped with polyvinylpyrrolidone. *Phys. Status Solidi B 246* **2009**, *10*, 2333–2336. [CrossRef]
26. Zhang, J.-H.; Ding, J.-W.; Cao, J.-X.; Zhang, Y.-L. Infrared, visible and ultraviolet absorptions of transition metal doped ZnScrystals with spin-polarized bands. *J. Solid State Chem.* **2011**, *184*, 477–480. [CrossRef]
27. Tablero, C. Electronic and magnetic properties of ZnS doped with Cr. *Phys. Rev. B* **2006**, *74*, 195203. [CrossRef]